

Sedimentation effects on particle position and inertial deposition in 90° circular bends

Sara Vahaji^a, Hien Nguyen^b, Yidan Shang^b, Kiao Inthavong^{b,*}

^a*School of Engineering, Deakin University, Geelong, Victoria 3217, Australia*

^b*Mechanical & Automotive Engineering, School of Engineering, RMIT University, Bundoora, Victoria 3083, Australia*

Abstract

Laminar fluid-particle flows in bend geometries are present in many industrial, pharmaceutical, and biomedical applications. Particle deposition has been studied extensively; however, little attention has been paid to the effect of particle sedimentation on particle position and deposition in different pipe geometry combinations. This study presented a comprehensive analysis of sedimentation effects on particle flow behaviour in 90° circular pipe bends of micron particles in laminar pipe flows. Pipe geometry combinations consisted of eight pipe diameters, nine bend radii, and 30 particle diameters in a range of 1 to 100 μm . The results demonstrated the locations of particles that sedimented to the bottom half of the straight pipe section, and the particle positions upstream from the pipe bend entrance, which was no longer in a fully developed profile. These new locations represent the effects of gravity, pulling the particles down. While obtaining these positions can be found through CFD analysis, we proposed an analytical solution to predict the particle trajectory from different release locations that would help to identify the initial particle distribution at locations upstream to the bend, to obviate the need for long upstream straight pipe sections in the CFD analysis.

Keywords: Particle deposition, sedimentation, pipe bend, micron particles, CFD, computational fluid dynamics

*Corresponding Author: kiao.inthavong@rmit.edu.au

Introduction

Dilute gas-particle flows in pipe bends are prevalent in many industries, including pharmaceutical, building ventilation, and oil and gas, where the particles are transported in pipes, ducts, or the human respiratory tract. In the human respiratory tract, pipe-like bends are observed at different locations: in the nostril to the main nasal passage, at the nasopharynx or the transition from the oral to oropharynx (Yousefi et al., 2015; Storey-Bishoff et al., 2008; Inthavong, 2020; Li et al., 2013). To improve the drug delivery efficiency, optimized designs exploiting gas-particle flow dynamics are needed; therefore, enhancing the knowledge of particle deposition in bends is critical.

Particle deposition in pipes is influenced by flow rate, cross-sectional pipe area, and bend geometry. The pipe diameter could be as small as 0.001m (air sampling instruments) or as large as 1m (transporting fluids in industry), and the pipe bend can exhibit different curvatures. In many studies, the Stokes (St) number is reported as the influencing parameter on the particle deposition (Shi et al., 2007). Other investigations (Grgic et al., 2004b) showed that Reynolds (Re) number also impacts the deposition process. These two parameters put together and recast as the inertial parameter, $IP = d_p^2 Q$ where d is the aerodynamic particle diameter (Inthavong et al., 2013), and Q is the flow rate, which is relevant for micron particle deposition that is susceptible to the inertial deposition mechanism. In addition to St and Re numbers, Dean (1928) identified that the curvature ratio in bends has a direct impact on the particle deposition as well. The Dean (De) number was introduced as a function of Re number and the curvature ratio, where $De = Re/\sqrt{R_o}$. The curvature ratio is $R_o = R_b/R_p$ where R_b is the bend radius, and R_p is the pipe radius. However, all St, Re, and De numbers account only for impaction, and not the gravitational settle-

ment (sedimentation). Nicolaou (2018) introduced the Froude number, the ratio of the gravitational settling velocity to the fluid velocity, as the dimensionless number that accounts for both impaction and gravitation.

To enhance the knowledge in the deposition process, many experimental (Johnston and Muir, 1973; Johnston et al., 1977; Vahaji et al., 2015; Landahl and Herrmann, 1949; Safari Pour et al., 2018; Peters and Leith, 2004; Pui et al., 1987) and numerical (Arsalanloo and Abbasalizadeh, 2017; Berrouk et al., 2007; Breuer et al., 2006; Cong et al., 2017; McFarland et al., 1997; Vahaji et al., 2018, 2019; Peng and Cao, 2016; Pilou et al., 2011; Tian et al., 2008; Tsai and Pui, 1990; Wilson et al., 2011) studies have been performed. The effects of particle size and flow rate on deposition was studied (Cheng et al., 1999; Grgic et al., 2004a), as well as the effect of pipe bend geometry (Grgic et al., 2004a; Heenan et al., 2004; Nicolaou and Zaki, 2013), and different Reynolds numbers and curvature ratios (Johnston and Muir, 1973; Johnston et al., 1977; Landahl and Herrmann, 1949; Pui et al., 1987).

Many investigations have also proposed analytical solutions for particle deposition (Cheng and Wang, 1975, 1981; Johnston et al., 1977; McFarland et al., 1997; Peng and Cao, 2016; Peters and Leith, 2004; Tsai and Pui, 1990; Wilson et al., 2011); but these are limited to the range of parameters investigated and may not translate well for general configurations. The author's previous work (Inthavong, 2019) provided a correlation for micron particle deposition in pipe bends given as $\eta = 2/\pi \tan^{-1} (20.976St^{2.253})$, where the Stokes number was defined as, $St = \tau U_0/R_p$; τ is the particle relaxation time, U_0 is the mean velocity, and R_p is the pipe radius. The results were based on a large data set that covered most common geometry arrangements and flow regimes in laminar flow. This included pipe diameters from 0.005m to 0.100m pipe diameters; bend radii from 0.006m to 0.070m; and Reynolds

numbers of 400 to 2000 Reynolds numbers.

In the presence of gravity, particle deposition in a pipe bend becomes sensitive to the upstream distance of particle release. [Pich \(1973\)](#) developed an analytical solution to predict the sedimentation deposition, but referred to it as the precipitation efficiency, in an elliptical and a circular channel as a function of a new parameter ϵ . Similarly, a parameter, $k = (3/4)St(gL/v_0^2)$ that could be used to characterize the deposition was proposed in [Finlay and Martin \(2008\)](#) based on an analytical solution for the gravitational settling of particles in a tubular geometry.

This study builds upon the past work that has been achieved. For example, particle penetration in a laminar flow tube was investigated ([Alonso et al., 2016](#)). Particle deposition in pipe bends have been studied extensively and for laminar flows some analytical solutions have been revealed, but under many assumptions that include an idealized flow. This includes [Cheng and Wang \(1975, 1981\)](#) which provided analytical solutions to the motion (of [Mori and Nakayama \(1967\)](#)) and inertial deposition of particles in a bend, while [Davies \(1973\)](#) demonstrated sedimentation in a straight pipe. More recently [Yu et al. \(2021\)](#) reported diffusion and sedimentation effects in a straight, and [Inthavong \(2019\)](#)'s results also showed scattered data due to sudden sedimentation from the different upstream release locations.

Previous studies for deposition in a 90-deg pipe bends [Li et al. \(2013\)](#); [Guo et al. \(2020\)](#); [Inthavong \(2019\)](#); [Breuer et al. \(2006\)](#) used varying upstream particle positions where in real applications, heavy particles are influenced by sedimentation and the longer upstream distances will alter the particle positions as they enter the pipe bend section. This study aims to provide a technique to omit the upstream location by solving the sedimentation problem and comparing the solution with CFD predicted results. This will allow identification of particle positions due to sedi-

mentation from the upstream straight pipe region, that end up affecting deposition efficiencies. This was achieved by integrating an upstream horizontal straight pipe section to the pipe 90° bend and considered the sedimentation effects on the overall deposition preceding the bend. CFD simulations of fluid-particle flow with $Re = 1000$ for a combination of eight pipe diameters, nine bend curvatures, and thirty micron particles in the range of 1 to 100 μm were performed to obtain an extensive data set for establishing deposition correlations.

The results are expected to serve as a reference point for future analysis of sedimentation and its effect on particle locations that influence deposition on a wall, while the analytical solution will be used as inlet boundary conditions for particle locations that consider sedimentation effects from upstream locations. This provides significant benefits for applications that exhibit long upstream locations.

1. Method

1.1. Geometry Model

Pipe geometries were created from combinations of pipe diameter D , with pipe bend radius R_b . For any combination, the geometry is physically constrained by $R_b > D/2$ (i.e. the bend radius must be greater than the pipe radius) otherwise it is physically impossible since the bend radius length R_b from the horizontal and vertical pipe sections crosses over (see Fig 1a). Eight pipe diameters ranging from 0.005m to 0.100m combined with nine bend radii ranging from 0.006m to 0.070m were created (Table 1). A total of 48 cases were made after the constraint $R_b > D/2$.

The inlet and outlet straight sections connected to the bend were made sufficiently long to avoid secondary flow influence from the bend curvature on the particle trans-

Pipe Diameter, D :	5, 8, 10, 20, 40, 60, 80, 100
Bend Radius, R_b :	6, 8, 10, 15, 20, 30, 40, 55, 70
and individual cases:	$D_1 = 5.031$, $R_{b1} = 14.3355$
(for comparison against	$D_2 = 8.51$, $R_{b2} = 23.828$
existing experiments)	$D_3 = 3.95$, $R_{b3} = 11.275$

Table 1: Pipe geometry configuration (units in millimetres)

port. Both [Berrouk et al. \(2007\)](#) and [Breuer et al. \(2006\)](#) applied a straight inlet section of 1D (one pipe diameter length) and a straight outlet section of 2D (two diameter lengths) to avoid disturbance on the flow in the bend. [Röhrig et al. \(2015\)](#) used 2.5D upstream and 1.5D downstream, while [Zhang et al. \(2012\)](#) used 3D lengths. [Wilson et al. \(2011\)](#) used 10D to represent the entrance length, but this was because the particles were uniformly distributed at the inlet. The entrance length was sufficiently long to allow the fluid and particles to fully develop over the entrance region. In this study, the straight pipe sections were set to 7D for the inlet and 3.5D for the outlet which was sufficiently long to avoid an abrupt termination of the flow (Fig 1a). The influence of bend curvature on the upstream flow preceding the bend is expected to increase as the curvature ratio decreases to 1, i.e. $R_o \rightarrow 1$.

The computational mesh used an octagonal block centred structured mesh, biased near the walls (Fig 1c). A mesh independence test was performed with three meshed models where the number of cells in each coordinate is given in Table 2. The medium-mesh model was confirmed as independent through velocity profiles in pipe bends of $R_b = 2.8D$ (the velocity profile results are shown later in the Results section). The

mesh density depended on the number of cells created along the pipe circumference, its radial distribution (biased towards the wall boundary), and distribution along its streamwise length. The total number of cells varied based on a constant distance between each cell along the bend curvature in the streamwise direction. Therefore, the largest pipe diameter with the largest bend radius produced the greatest number of cells. The number of cells in the radial and circumferential directions were constant. In the streamwise direction, the number of cells was equal to the straight inlet section (75 cells for medium mesh) plus the straight outlet section (45 cells for medium mesh) plus the number of cells in the bend which varied based on bend curvature defined as $(40 + R_b/D \times 16)$. For example, this produced 176 cells for $R_b/D = 1.0$ and 205 cells for $R_b/D = 2.8$ for the Medium mesh settings.

Table 2: Mesh configuration defined by the number of cells in the cross-section (radial, and circumferential directions) and along the streamwise direction.

	number of cells			Example $R_b = 0.028, D = 0.01$	
	radial	circ.	stream.	stream.	Total
Coarse	24	75	$50 + (26 + R_b/D \times 10) + 30$	134	241,200
Medium	36	112	$75 + (40 + R_b/D \times 16) + 45$	205	825,754
Fine	50	145	$100 + (58 + R_b/D \times 26) + 60$	291	2,108,300

1.2. Fluid-particle modelling

A laminar flow was used for the range of Reynolds numbers, and a fully developed profile was applied at the entrance,

$$u(r) = 2U_{ave} \left(1 - \frac{r^2}{R^2} \right) \quad (1)$$

was used at the inlet for these studies, where U_{ave} is the average velocity, r is the radial distance from the pipe centre, and R is the pipe radius. Reynolds number is kept at $Re = 1000$ for all the cases, so for the smallest pipe diameter, $D_{min} = 0.005\text{m}$, maximum velocity of $U_{ave} = 2.92\text{m/s}$ occurs. Similarly, the minimum velocity, $U_{ave} = 0.15\text{m/s}$, occurs in the largest pipe diameter, $D_{max} = 0.1\text{m}$. The fluid was treated as a continuous Eulerian phase and modelled using the CFD commercial code Ansys-Fluent v19v3. The discretisation schemes used were: second order for the pressure and momentum equation, and solving with the coupled approach. Particles were modelled using the Discrete Phase Model, which simultaneously tracks individual particles through the flow field. The particle phase was assumed dilute (less than 10% volume fraction) such that the particle motion did not influence the fluid motion. The particle either reached the pipe wall where it was assumed to deposit, or escaped through the computational domain via the outlet.

The particle equation of motion is given by

$$m_p \frac{d\vec{u}_p}{dt} = m_p \frac{\vec{u} - \vec{u}_p}{\tau_r} + m_p \frac{\vec{g}(\rho_p - \rho_g)}{\rho_p} + \vec{F} \quad (2)$$

where m_p is the particle mass, \vec{u} is the fluid phase velocity, \vec{u}_p is the particle velocity, ρ_g is the gas (air) density, ρ_p is the density of the particle, \vec{F} is an additional force, $m_p \frac{\vec{u} - \vec{u}_p}{\tau_r}$ is the drag force, τ_r is the droplet or particle relaxation time calculated by

$$\tau_r = \frac{\rho_p d_p^2}{18\mu C_d Re} \quad (3)$$

here, μ is the molecular viscosity of the fluid, d_p is the particle diameter, and Re is

the relative Reynolds number, which is defined as

$$Re \equiv \frac{\rho d_p |\vec{u}_p - \vec{u}|}{\mu} \quad (4)$$

Also, the drag coefficient is taken from [Morsi and Alexander \(1972\)](#) defined by

$$C_d = a_1 + \frac{a_2}{Re_p} + \frac{a_3}{Re_p} \quad (5)$$

where the a_1 , a_2 , and a_3 are empirical constants for smooth spherical particle over different ranges of particle Reynolds number. The particle Stokes number is

$$St = \tau \frac{U_o}{L_o} \quad (6)$$

U_o/L_o is the fluid time scale that is defined by the ratio of a characteristic velocity to a characteristic length, here it is taken as U_{ave}/R , where R is the pipe radius (note that sometimes this length is taken as the pipe diameter).

Thirty particle diameters were considered, and for completeness and consistency, the entire range of diameters was used for all cases, despite some particles producing similar flow behavior. The diameters were: all (integers) between 1 to 20, 23, 25, 30, 35, 40, 45, 50, 60, 80, 100, giving thirty diameter sizes per pipe configuration. The deposition efficiency reported was for deposition in the bend section only, defined as

$$\eta = \frac{\text{number of particles depositing in bend}}{\text{number of particles entering the bend}} \quad (7)$$

thus, particle losses in the straight pipe section preceding the bend were excluded.

Particles were introduced at the inlet with an initial velocity matching the fully developed laminar flow profile in Eq (1). The total number of particles was tested for statistical independence by progressively increasing from 5000 particles to 50,000 and determining the deposition efficiency in one pipe condition. The final number for statistical independence was 30,000 particles. Deposition is based on parcel/particle mass depositing on the walls.

1.3. Sedimentation

Particle motion influenced by sedimentation was approximated in the mid-plane by adopting a force balance equation (Fig.2). Assuming a Stokes drag, and subjected to gravity, the particle motion in the vertical axis (y-axis) is given by:

$$\frac{dv_p(t)}{dt} = -C_1 v_p(t) - \beta g \quad (8)$$

where $v_p(t) = \frac{dy(t)}{dt}$. The solution for the vertical displacement is

$$y_p(t) = y_0 + \frac{\beta g (1 - e^{-C_1 t} - C_1 t)}{C_1^2} \quad (9)$$

where y_0 is the initial vertical position, $\beta = \left(1 - \frac{\rho_0}{\rho}\right) g$.

The assumed Stokes drag law of $C_d = \frac{24}{Re}$ simplifies C_1 to the following

$$C_1 = \frac{18\mu}{\rho d_p^2}$$

which is essentially the inverse of the particle relaxation time, e.g., $C_1 = 1/\tau$. For a particle moving near a wall, the drag force varies with the distance of the particle from the surface, and the drag force is adjusted to account for drag acting on a particle moving toward a wall under the creeping flow. This is given by [Brenner \(1961\)](#) as:

$$C_d = \frac{24}{Re} A$$

where

$$A = 1 + \frac{d}{2h}$$

while for a particle moving parallel to the wall, [Faxén \(1922\)](#)'s equation gives

$$A = \left(1 - \frac{9}{16} \left(\frac{d}{2h} \right) + \frac{1}{8} \left(\frac{d}{2h} \right)^3 - \frac{45}{256} \left(\frac{d}{2h} \right)^4 - \frac{1}{16} \left(\frac{d}{2h} \right)^5 \right)^{-1}$$

This suggests the particle relaxation time also needs adjustment and this value is tuned against the CFD results, and for now is simply given as

$$C_1 = \frac{18\mu}{\rho d^2} A_1 \tag{10}$$

Particle motion in the streamwise direction (see 2) was determined by

$$\frac{dw_p(t)}{dt} = C_1 [w_f(t) - w(t)] \quad (11)$$

The solution for the horizontal displacement is therefore,

$$\begin{aligned} z_p(t) = & C_6 - \frac{C_2 C_4^2 e^{-2C_1 t}}{2C_1} - C_2 (-1 + C_3^2 + 4C_3 C_4 + 5C_4^2) t \\ & + C_1 C_2 C_4 (C_3 + 2C_4) t^2 - \frac{1}{3} C_1^2 C_2 C_4^2 t^3 \\ & + \frac{e^{-C_1 t} \{-C_5 + C_2 C_4 [C_1^2 C_4 t^2 - 2C_3 (1 + C_1 t)]\}}{C_1} \end{aligned} \quad (12)$$

where the constants C_1 to C_6 are:

$$\begin{aligned} C_1 &= \frac{18\mu}{\rho d^2} A_1 \\ C_2 &= 2w_A \\ C_3 &= \frac{y_0}{R} \\ C_4 &= \frac{\beta g}{RC_1^2} \\ C_5 &= 2w_A \left(1 - \frac{y_0^2}{R^2}\right) + C_2 (-1 + C_3^2 + 4C_3 C_4 + 4C_4^2) \\ C_6 &= \frac{C_2 C_4 (4C_3 + C_4) + 2C_5}{2C_1} \end{aligned}$$

2. Results

2.1. Velocity Profiles

Fig 3 presents the radial profiles of velocity magnitude along lines A-A' (Fig 3a), and B-B' (Fig 3b) taken at $\theta = 45^\circ$ and $\theta = 90^\circ$. In this figure, our results for $R_o = 5.6$

are compared to numerical results – based on a Finite Volume computational model – from Nicolaou and Zaki (2016). Fig 3a shows that at $\theta = 45^\circ$, due to the inertial forces the velocity profile is skewed towards the outer wall. At the bend, secondary flow forms and continues to the bend exit (at $\theta = 90^\circ$) where another peak with less magnitude is formed near the inner wall. Line B-B' (Fig 3b) presents a symmetrical velocity profile for both $\theta = 45^\circ$ and $\theta = 90^\circ$ locations. Due to the vortices that are shaped following the secondary flow, the velocity profile slightly changes at $\theta = 90^\circ$, which is compatible with the observations at line A-A'.

Fig 4 shows the flow development across the pipe bend for $R_o = 2.0$ (sharp bend) and $R_o = 14.0$ (long bend). The effect of secondary flow on the streamlines and vortex structures are depicted, where the streamlines split in the middle and diverge to the sides to produce the vortex structures. The effect of secondary flow is evident in the streamlines. In the sharp bend, disturbances in the fully developed laminar velocity profile occur well before the inlet of the bend section. In contrast, the disturbances in the long bend are contained within the pipe bend itself. This suggests a minimum upstream distance should be considered in pipe bends that have high Dean numbers.

To better understand the flow field for different curvature ratios, velocity contours were extracted in the pipe bend at angles $\theta = 0^\circ, 22.5^\circ, 45^\circ, 67.5^\circ,$ and 90° shown in Fig 5 pipe bend ratios of $R_o = 1.2, 1.6, 2.0, 3.0, 4.0, 6.0, 8.0, 11.0,$ and 14.0 . Since the inertia is constant (constant Re number), the differences in the cases are caused only by centrifugal forces by changing the curvature ratio.

The cross-section at the bend inlet plane, $\theta = 0^\circ$, shows the flow field is affected by sharper pipe bends (e.g. when R_o is small, ≤ 2) depicted in the pipe bends with a lower curvature ratio. The fully developed profile (where the peak flow is at the centre of the pipe) is altered to having lower velocities at the inner wall

and peak velocity on the outer wall (top of each cross-section). The secondary flow effects are diminished with increasing curvature ratio. In sharp bends, the short pipe circumference prohibits the development of Dean vortices where become are not present until the bend exit at $\theta = 90^\circ$. With the longer bends, the centrifugal forces have sufficient distance to transfer the momentum into the secondary flow, leading to Dean vortices occurring progressively earlier (with increasing R_o) in the pipe bends, i.e. occurring at cross-sections closer to the pipe bend inlet.

2.2. Particle Deposition Efficiency

Deposition efficiency for three pipe combinations of R_b , and D (5.03 mm, 3.95 mm, 8.51 mm) were used to obtain $R_o = 5.5, 5.6$, and 5.7 following the experimental setup of [Pui et al. \(1987\)](#). The deposition efficiency in the pipe bend for $Re=1000$ was compared against studies in literature, with gravity being considered (Fig 6a) and without gravity (Fig 6b). There was a good comparison with the literature, especially for higher Stokes numbers: considering gravity and with [Pui et al. \(1987\)](#), and neglecting gravity with [Breuer et al. \(2006\)](#).

The influence of sedimentation can be depicted by varying the particle release locations (from 1D, 3D, and 5D downstream of the inlet) and tracking the particle positions in planes at sequential pipe diameter distances downstream. Two distinct particle sizes, $4\mu\text{m}$ and $30\mu\text{m}$ representing both low and high inertial properties and light and heavy particles were investigated. Fig 7 shows the particle positions inside the pipe and wall deposition, with each particle coloured by velocity in a pipe with a diameter of 0.01m and a radius of 0.1m

Fig 7a demonstrates the behaviour of $4\mu\text{m}$ particles released from different upstream locations (at 1D, 3D, and 5D). The cross-section planes in the pipe inlet section show

the particles maintain an entrained state within the transporting air. Particles at the top of each plane remain close to the top pipe surface, suggesting negligible sedimentation effects. Particle deposition on the pipe surface is sparse and found only in the bottom half of the pipe inlet section and the inner pipe bend section. In the pipe bend section, the particles continue to behave like a gas tracer moving with the air and tracing out the Dean vortex patterns. The outlet plane depicts a high number of particles escaping for all release locations. This suggests that low inertial particles are insensitive to sedimentation effects, and therefore the upstream release location are negligible for the distances tested up to $7D$ in length.

Conversely, the behaviour of $30\ \mu\text{m}$ particles is sensitive to the upstream release location (Fig 7b) due to the influence of sedimentation. The cross-section planes in the pipe inlet section show the particles have descended and the top-most particles of each plane are clearly below the top pipe surface. Particle deposition on the bottom surface of the pipe inlet section is more concentrated. Deposition at the pipe bend section occurs on the outer pipe wall suggesting inertial impaction. In the pipe bend section, the number of particles travelling in the pipe is reduced. The outlet plane depicts a very sparse pattern suggesting a small number of particles escaping for all release locations. This indicates that $30\ \mu\text{m}$ particles are sensitive to sedimentation, and the upstream release location has a significant influence on the particle distribution downstream.

Fig 8 demonstrates the effects of greater Dean number flows where the pipe bend is shortened by a factor of four (e.g., from $R_b = 0.04\text{m}$ to $R_b = 0.01\text{m}$). In both cases, the effects of sedimentation for both 4 and $30\ \mu\text{m}$ are the same. For $30\ \mu\text{m}$ particles, significant impaction occurs on the outer pipe bend wall, reducing the number of particles moving through the outlet pipe sections. As Dean number is increased, we

expect to see an increased intensity of the secondary flow, and this is depicted by the 4 μm particles moving through the pipe bend and the outlet plane. The intense secondary flow from the pipe bend penetrates the upstream pipe bend inlet locations (at the 7D location) where there is a small crescent of particles located above the main circular plane of particles.

The effect of particle release location on the deposition efficiency of the bend wall is given in Fig 9a, where the results in each panel show the pipe diameter change from 0.01m to 0.1m, and profiles are coloured by the particle release location for all the bend curvature ratios. The results show that an increase in the pipe diameter, regardless of the curvature ratio, the sedimentation effects increases. The deposition efficiency curve collapses due to fewer particles depositing on the wall bend, even for the particles that are released close to the bend (at location 6D). For particles released closer to the pipe bend inlet, deposition was due to inertial impaction on the outer wall.

The effect of bend curvature ratio on the deposition efficiency of the bend wall is given in Fig 9b where the colours represent different curvature ratios. An increase in the curvature ratio produces an increase in deposition efficiency. This suggests that in addition to the inertial impaction on the outer wall, the particles will deposit on the inner wall due to momentum loss in the higher curvature ratio pipes (e.g., longer pipe bends).

2.3. Particle Deposition and Sedimentation Analysis

To obtain an overall correlation, the data for all particle diameters and all cases were plotted (Fig 10). For pipe bend deposition efficiency the particle Stokes number was used as the normalising parameter, and for sedimentation, it was ϵ from Pich (1973).

Data points are semi-transparent and coloured by particle diameter, while the solid curve fit line was taken from [Inthavong \(2019\)](#) which is defined as $2/\pi \tan^{-1}(aSt^b)$. The curve fit captures the overall inertial impaction onto the pipe bend section. However, there is some scatter of the data, which is primarily limited to larger particles (coloured in red). The effects of sedimentation were evident in larger pipe diameters for large particles (shown in Fig 9) where the deposition and particle distribution in cross-section planes were unique based on upstream particle release locations. Therefore, the curve fit line from [Inthavong \(2019\)](#) to describe deposition efficiency (Fig 10a) has limitations in its ability to capture the effects of sedimentation on larger particles, i.e. greater than 20 μm , and that the upstream locations should be considered when the gravitational force is involved.

Sedimentation in the straight pipe inlet section (before the bend) was plotted for all particles in all pipes. The analytical curve for Fig 10b was from [Pich \(1973\)](#), defined as

$$2/\pi \left(2\epsilon\sqrt{1 - \epsilon^{2/3}} - \epsilon^{1/3}\sqrt{1 - \epsilon^{2/3}} + \arcsin \epsilon^{1/3} \right) \quad (13)$$

where $\epsilon = \frac{3}{4} \frac{V_s}{D} \frac{L}{U}$ is the dimensionless parameter, V_s is the stationary sedimentation velocity of particles, and L is the length of the inlet section. The deposition efficiency is dominated by the larger particles, while particles smaller than 20 μm having less than 0.15 deposition efficiency. The analytical curve fit equation predicts the particle sedimentation on the upper range and in most cases, overpredicts the simulation results.

The particle trajectories for 4 μm , 15 μm , and 50 μm in three pipe geometries (short pipe bend, long pipe bend, large pipe diameter) and released from four heights (R , $R/2$, 0, and $-R/2$) in the pipe are presented in Fig 11. The CFD results were plotted

in black lines. A comparison was made with the analytical solution given in Eqn. 9 where A_1 in the vertical motion (Eqn.10) was $2/3$, while in the streamwise motion (Eqn.10) was 1. The trajectories from Eqn. 9 were coloured red, blue, green and pink, and overlaid onto the CFD results which demonstrated very good matching of results. Small deviations were found at the end of the straight pipe section at a distance $7D$ from the inlet where secondary flow effects influenced the flow field.

The trajectories demonstrate the amount of vertical drop due to sedimentation over the straight pipe section. For the larger pipe diameter, the average flow velocity was reduced to maintain the same Reynolds number. Therefore, the sedimentation is substantially greater, particularly for $15\mu\text{m}$ and $50\mu\text{m}$ particles. For the pipe diameters of $D = 0.01\text{m}$ $50\mu\text{m}$ particles released from the top of the pipe, at R , drop much faster than the particles released at $R/2$ because the flow field exhibits a fully developed laminar velocity profile. The trajectories indicate the top-most bounded particle positions found in the downstream planes (visualised in Fig. 7b and 8b) after sedimentation. As a result, the analytical equation could determine the particle positions at a location downstream from any upstream location that could be very long, e.g., $10D$, $20D$, or $40D$. This can allow a standard straight pipe section length to be used, typically $3D$ in length with a fully developed profile and the initial particle positions due to upstream sedimentation is defined by Eqn. 9 and Eqn. 11.

3. Conclusion

In this study, the effect of sedimentation in laminar fluid-particle flows in pipe bend combinations is investigated. Particles ranging from 1 to $100\mu\text{m}$ were released at cross-sections planed with a fully developed laminar profile. Different release cross-section locations from the inlet were evaluated to analyse particle deposition on the

pipe surface. The findings are especially important for the applications where long upstream locations are present. A detailed study identifying the particle positions affected by sedimentation from upstream locations will reduce the computational cost by removing the need for CFD modelling of the upstream pipe sections. The analytical solution can be used to determine the initial particle positions in the straight pipe section, at different upstream locations from the pipe bend entrance.

The results showed that small particles ($4\ \mu\text{m}$) travelled with the flow field unless they were located in low-velocity regions (such as the near wall, or in the recirculation zones). In contrast, larger particles were influenced by inertial impaction and sedimentation. Releasing particles close to the bend inlet were subjected to secondary flow effects in high Dean numbered flows, suggesting that two to three pipe diameters of a straight section should be used. In pipes with larger diameters, the average flow velocity was reduced to maintain a consistent Reynolds number, and this led to increased particle sedimentation. This was also found in bends with higher curvatures, where the particles deposited on the inner wall of the bend due to momentum loss.

Visualisation of the particle positions through the pipe cross-sections demonstrated the influence of sedimentation on the larger particles, while the smaller particles traced out the flow field effectively, particularly the Dean vortices after the pipe bend. An analytical solution to particle motion in a straight pipe was proposed which predicted the same particle trajectories found in the CFD simulations. The equation provides a technique to predict particle positions downstream from the inlet of very long straight pipes and therefore, gives computational efficiencies by avoiding the CFD modelling of an entire straight section where particle deposition in pipe bends are of interest.

4. Acknowledgements

The authors gratefully acknowledge the financial support provided by Deakin University startup funds.

References

- Alonso, M., Carsí, M., Huang, C.H., 2016. Using the fully developed concentration profile to determine particle penetration in a laminar flow tube. *Journal of Aerosol Science* 97, 34–37. URL: <http://www.sciencedirect.com/science/article/pii/S0021850216300829>, doi:<https://doi.org/10.1016/j.jaerosci.2016.04.002>.
- Arsalanloo, A., Abbasalizadeh, M., 2017. Numerical study on deposition of particles in a 90° bend in the presence of swirling flow using eulerian-lagrangian method. *Powder Technology* 320, 285–294. URL: <http://www.sciencedirect.com/science/article/pii/S0032591017305867>, doi:<https://doi.org/10.1016/j.powtec.2017.07.050>.
- Berrouk, A.S., Laurence, D., Riley, J.J., Stock, D.E., 2007. Stochastic modelling of inertial particle dispersion by subgrid motion for les of high reynolds number pipe flow. *Journal of Turbulence* 8, N50. URL: <http://www.informaworld.com/10.1080/14685240701615952>.
- Brenner, H., 1961. The slow motion of a sphere through a viscous fluid towards a plane surface. *Chemical Engineering Science* doi:[10.1016/0009-2509\(61\)80035-3](https://doi.org/10.1016/0009-2509(61)80035-3).
- Breuer, M., Baytekin, H.T., Matida, E.A., 2006. Prediction of aerosol deposition in 90o bends using les and an efficient lagrangian tracking method. *Journal of Aerosol Science* 37, 1407–1428. URL: <http://www.sciencedirect.com/science/article/B6V6B-4JKYWH8-1/2/ca797d19d783c6bdf80e3f8d4c7e4914>.
- Cheng, Y.s., Wang, C.s., 1975. Inertial deposition of particles in a bend. *Journal of Aerosol Science* 6, 139–145. URL: <http://www.sciencedirect.com/science/article/pii/0021850275900075>, doi:[http://dx.doi.org/10.1016/0021-8502\(75\)90007-5](http://dx.doi.org/10.1016/0021-8502(75)90007-5).
- Cheng, Y.S., Wang, C.S., 1981. Motion of particles in bends of circular pipes. *Atmospheric Environment* (1967) 15, 301–306. URL: <http://www.sciencedirect.com/science/article/pii/0004698181900329>, doi:[https://doi.org/10.1016/0004-6981\(81\)90032-9](https://doi.org/10.1016/0004-6981(81)90032-9).
- Cheng, Y.S., Zhou, Y., Chen, B.T., 1999. Particle deposition in a cast of human oral airways. *Aerosol Science and Technology* 31, 286–300.
- Cong, X.C., Yang, G.S., Qu, J.H., Zhao, J.J., 2017. A model for evaluating the particle penetration efficiency in a ninety-degree bend with a circular-cross section in laminar and turbulent flow regions. *Powder Technology* 305, 771–781. URL: <http://www.sciencedirect.com/science/article/pii/S0032591016307677>, doi:<https://doi.org/10.1016/j.powtec.2016.10.074>.

- Davies, C., 1973. Diffusion and sedimentation of aerosol particles from poiseuille flow in pipes. *Journal of Aerosol Science* 4, 317–328.
- Dean, W., 1928. Lxxii. the stream-line motion of fluid in a curved pipe (second paper). *The London, Edinburgh, and Dublin Philosophical Magazine and Journal of Science* 5, 673–695.
- Faxén, H., 1922. Der widerstand gegen die bewegung einer starren kugel in einer zähen flüssigkeit, die zwischen zwei parallelen ebenen wänden eingeschlossen ist. *Annalen der Physik* 373, 89–119. URL: <https://onlinelibrary.wiley.com/doi/abs/10.1002/andp.19223731003>, doi:<https://doi.org/10.1002/andp.19223731003>, arXiv:<https://onlinelibrary.wiley.com/doi/pdf/10.1002/andp.19223731003>.
- Finlay, W.H., Martin, A.R., 2008. Recent advances in predictive understanding of respiratory tract deposition. *Journal of Aerosol Medicine and Pulmonary Drug Delivery* 21, 189–206.
- Grgic, B., Finlay, W., Burnell, P., Heenan, A., 2004a. In vitro intersubject and intrasubject deposition measurements in realistic mouth–throat geometries. *Journal of Aerosol Science* 35, 1025–1040.
- Grgic, B., Finlay, W., Heenan, A., 2004b. Regional aerosol deposition and flow measurements in an idealized mouth and throat. volume 35. doi:[10.1016/S0021-8502\(03\)00387-2](https://doi.org/10.1016/S0021-8502(03)00387-2).
- Guo, J., Chen, Z., Shen, B., Wang, J., Yang, L., 2020. Numerical study on characteristics of particle deposition efficiency on different walls of 90° square bend. *Powder Technology* 364, 572–583.
- Heenan, A., Finlay, W., Grgic, B., Pollard, A., Burnell, P., 2004. An investigation of the relationship between the flow field and regional deposition in realistic extra-thoracic airways. *Journal of aerosol science* 35, 1013–1023.
- Inthavong, K., 2019. A unifying correlation for laminar particle deposition in 90-degree pipe bends. *Powder Technology* 345, 99–110. URL: <https://www.scopus.com/inward/record.uri?eid=2-s2.0-85059574958&doi=10.1016%2Fj.powtec.2018.12.095&partnerID=40&md5=e5b17e90a0b4ef0252dd89788e2325ca>, doi:[10.1016/j.powtec.2018.12.095](https://doi.org/10.1016/j.powtec.2018.12.095).
- Inthavong, K., 2020. From indoor exposure to inhaled particle deposition: A multiphase journey of inhaled particles. *Experimental and Computational Multiphase Flow* doi:[10.1007/s42757-019-0046-6](https://doi.org/10.1007/s42757-019-0046-6).
- Inthavong, K., Mouritz, A.P., Dong, J., Tu, J.Y., 2013. Inhalation and deposition of carbon and glass composite fibre in the respiratory airway. *Journal of aerosol science* 65, 58–68.
- Johnston, J., Isles, K., Muir, D., 1977. Inertial deposition of particles in human branching airways. volume 4 of *Inhaled Particles*. Pergamon Press, Oxford.
- Johnston, J., Muir, D., 1973. Inertial deposition of particles in the lung. *Journal of Aerosol Science* 4, 269–270.
- Landahl, H.D., Herrmann, R.G., 1949. Sampling of liquid aerosols by wires, cylinders, and slides, and the efficiency of impaction of the droplets. *Journal of Colloid Sci-*

- ence 4, 103–136. URL: <https://www.scopus.com/inward/record.uri?eid=2-s2.0-0003600955&doi=10.1016%2f0095-8522%2849%2990038-0&partnerID=40&md5=632d61dc987bf47e3b81485367251268>, doi:10.1016/0095-8522(49)90038-0.
- Li, X., Inthavong, K., Ge, Q., Tu, J., 2013. Numerical investigation of particle transport and inhalation using standing thermal manikins. *Building and Environment* doi:10.1016/j.buildenv.2012.11.014.
- McFarland, A.R., Gong, H., Muyschondt, A., Wentz, W.B., Anand, N.K., 1997. Aerosol deposition in bends with turbulent flow. *Environmental Science and Technology* 31, 3371–3377. URL: <http://dx.doi.org/10.1021/es960975c>, doi:10.1021/es960975c.
- Mori, Y., Nakayama, W., 1967. Study of forced convective heat transfer in curved pipes (2nd report, turbulent region). *International Journal of Heat and Mass Transfer* doi:10.1016/0017-9310(67)90182-2.
- Morsi, S., Alexander, A., 1972. An investigation of particle trajectories in two-phase flow systems. *Journal Fluid Mechanics* 55, 193–208.
- Nicolaou, L., 2018. Inertial and gravitational effects on aerosol deposition in the conducting airways. *Journal of Aerosol Science* 120, 32–51. URL: <https://www.scopus.com/inward/record.uri?eid=2-s2.0-85044523246&doi=10.1016%2fj.jaerosci.2018.03.003&partnerID=40&md5=4bf7260a6dcd8f2fc9a14ff99453109f>, doi:10.1016/j.jaerosci.2018.03.003.
- Nicolaou, L., Zaki, T., 2013. Direct numerical simulations of flow in realistic mouth–throat geometries. *Journal of Aerosol Science* 57, 71–87.
- Peng, W., Cao, X., 2016. Numerical simulation of solid particle erosion in pipe bends for liquid–solid flow. *Powder Technology* 294, 266–279. URL: <http://www.sciencedirect.com/science/article/pii/S0032591016300717>, doi:<https://doi.org/10.1016/j.powtec.2016.02.030>.
- Peters, T.M., Leith, D., 2004. Particle deposition in industrial duct bends. *The Annals of Occupational Hygiene* 48, 483–490. URL: <http://dx.doi.org/10.1093/annhyg/meh031>, doi:10.1093/annhyg/meh031.
- Pich, J., 1973. Theory of gravitational deposition of particles in fibrous aerosol filters. *Journal of Aerosol Science* 4, 217 – 226. URL: <http://www.sciencedirect.com/science/article/pii/0021850273900049>, doi:[https://doi.org/10.1016/0021-8502\(73\)90004-9](https://doi.org/10.1016/0021-8502(73)90004-9).
- Pilou, M., Tsangaris, S., Neofytou, P., Housiadas, C., Drossinos, Y., 2011. Inertial particle deposition in a 90° laminar flow bend: An eulerian fluid particle approach. *Aerosol Science and Technology* 45, 1376–1387. URL: <https://doi.org/10.1080/02786826.2011.596171>, doi:10.1080/02786826.2011.596171.
- Pui, D.Y.H., Romay-Novas, F., Liu, B.Y.H., 1987. Experimental study of particle deposition in bends of circular cross section. *Aerosol Science and Technology* 7, 301–315. URL: <https://doi.org/10.1080/02786828708959166>, doi:10.1080/02786828708959166.
- Röhrig, R., Jakirlić, S., Tropea, C., 2015. Comparative computational study of turbulent flow in a 90 pipe elbow. *International Journal of Heat and Fluid Flow* 55, 120–131.

- Safari Pour, S., Mohanarangam, K., Vahaji, S., Cheung, S.C.P., Tu, J., 2018. Visualisation of gas–liquid bubbly flows in a large diameter pipe with 90° bend. *Journal of Visualisation* 21, 585–596.
- Shi, H., Kleinstreuer, C., Zhang, Z., 2007. Modeling of inertial particle transport and deposition in human nasal cavities with wall roughness. *Journal of Aerosol Science* doi:[10.1016/j.jaerosci.2007.02.002](https://doi.org/10.1016/j.jaerosci.2007.02.002).
- Storey-Bishoff, J., Noga, M., Finlay, W.H., 2008. Deposition of micrometer-sized aerosol particles in infant nasal airway replicas. *Journal of Aerosol Science* doi:[10.1016/j.jaerosci.2008.07.011](https://doi.org/10.1016/j.jaerosci.2008.07.011).
- Tian, Z.F., Inthavong, K., Tu, J.Y., Yeoh, G.H., 2008. Numerical investigation into the effects of wall roughness on a gas-particle flow in a 90 degrees bend. *International Journal of Heat and Mass Transfer* 51, 1238–1250. doi:[10.1016/j.ijheatmasstransfer.2007.12.005](https://doi.org/10.1016/j.ijheatmasstransfer.2007.12.005).
- Tsai, C.J., Pui, D.Y.H., 1990. Numerical study of particle deposition in bends of a circular cross-section-laminar flow regime. *Aerosol Science and Technology* 12, 813–831. URL: <https://doi.org/10.1080/02786829008959395>, doi:[10.1080/02786829008959395](https://doi.org/10.1080/02786829008959395).
- Vahaji, S., Akbarzadeh, A., Date, A., Cheung, S.C.P., Tu, J., 2015. Study on the efficiency of a convergent-divergent two-phase nozzle as a motive force for power generation from low temperature geothermal resources. *Proceedings of the World Geothermal Congress 2015 Australia-New Zealand (WGC 2015)* 1, 1–14.
- Vahaji, S., Chen, L., Cheung, S.C.P., Tu, J., 2018. Numerical investigation on bubble size distribution around an underwater vehicle. *Applied Ocean Research* 78, 254–266.
- Vahaji, S., Han, J., Cheung, S.C.P., Yeoh, G.H., Tu, J., 2019. Numerical investigation on the bubble size distribution around naca0015 hydrofoil. *Ocean Engineering* 172, 59–71.
- Wilson, S.R., Liu, Y., Matida, E.A., Johnson, M.R., 2011. Aerosol deposition measurements as a function of reynolds number for turbulent flow in a ninety-degree pipe bend. *Aerosol Science and Technology* 45, 364–375. URL: <https://doi.org/10.1080/02786826.2010.538092>, doi:[10.1080/02786826.2010.538092](https://doi.org/10.1080/02786826.2010.538092).
- Yousefi, M., Inthavong, K., Tu, J., 2015. Microparticle Transport and Deposition in the Human Oral Airway: Toward the Smart Spacer. *Aerosol Science and Technology* doi:[10.1080/02786826.2015.1101052](https://doi.org/10.1080/02786826.2015.1101052).
- Yu, Y., Gao, Y., Kang, Y., 2021. Aerosol deposition in circular tubes with simultaneous consideration of diffusion and sedimentation. *Journal of Aerosol Science* 156, 105794.
- Zhang, P., Roberts, R.M., Bénard, A., 2012. Computational guidelines and an empirical model for particle deposition in curved pipes using an eulerian-lagrangian approach. *Journal of Aerosol Science* 53, 1–20. URL: <http://www.sciencedirect.com/science/article/pii/S0021850212000997>, doi:<https://doi.org/10.1016/j.jaerosci.2012.05.007>.

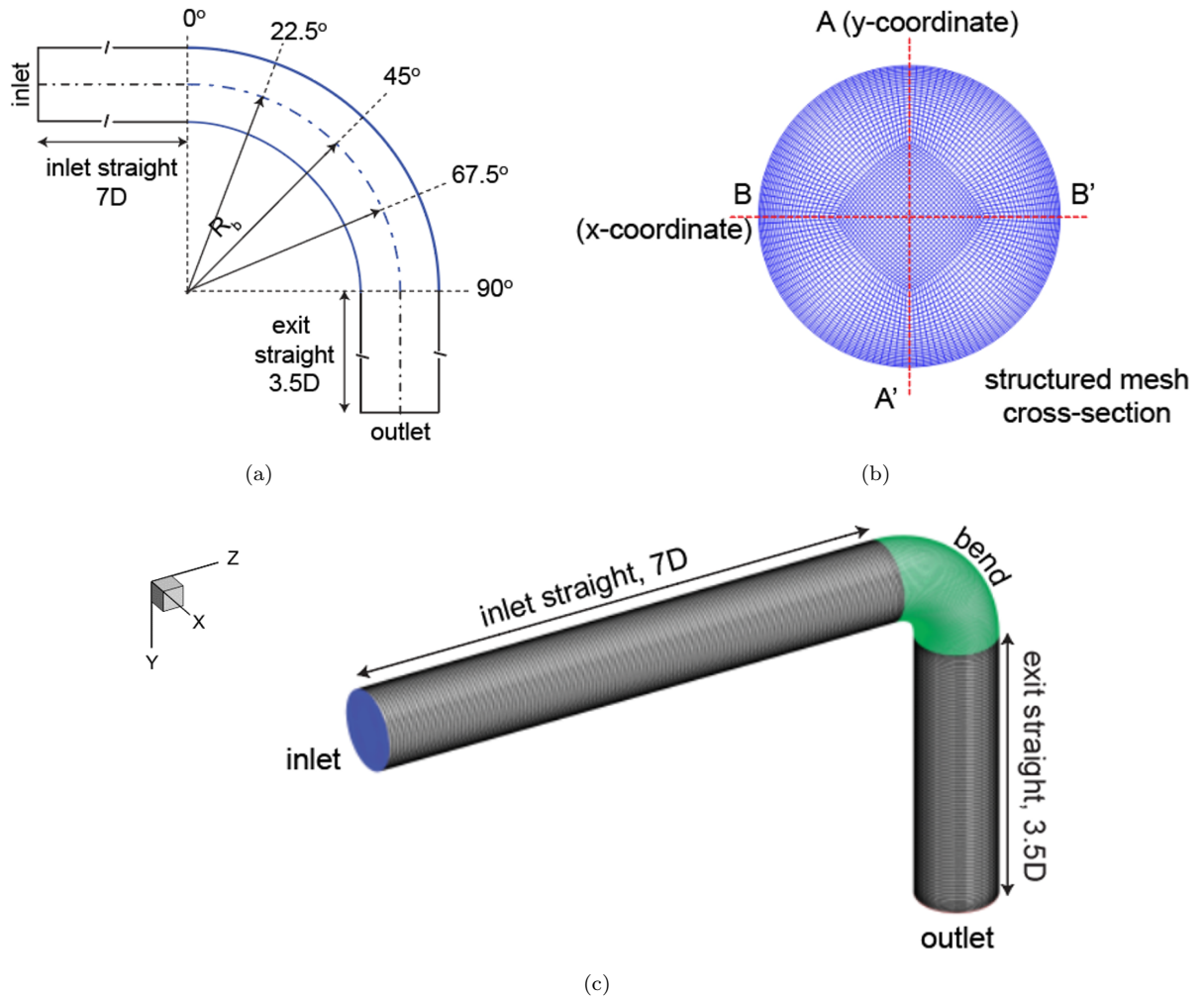


Figure 1: (a) Schematic of the circular pipe bend geometry for all cases where R_b and the pipe diameter, D varied. (b) Internal (cross-section) mesh which used O-grid block meshing, and concentration of cells near the wall. (c) Structured mesh on the external wall surface.

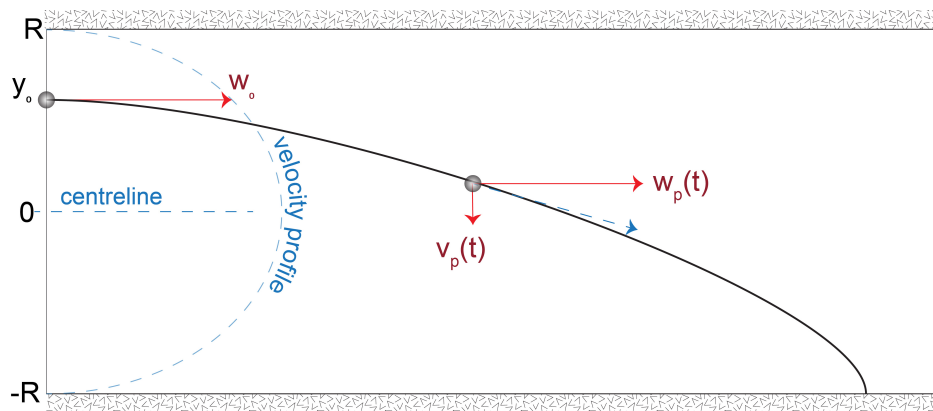
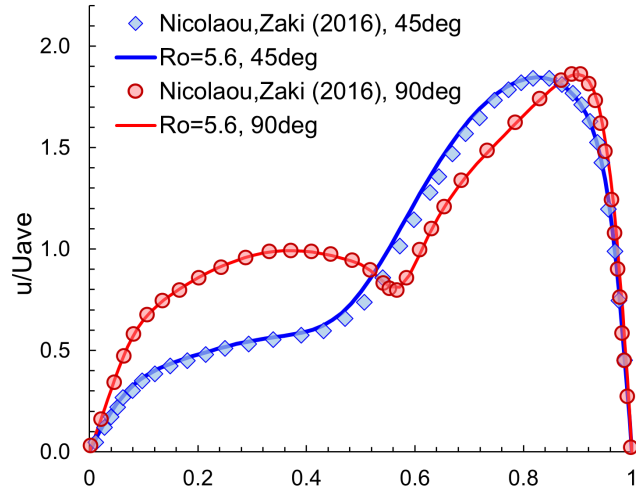
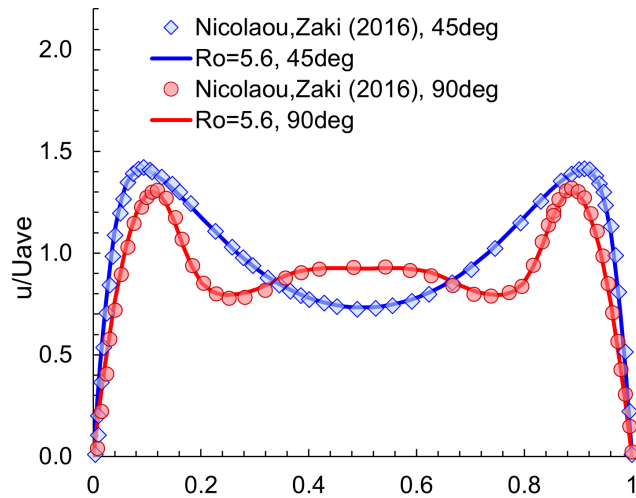


Figure 2: Schematic of the coordinate system for 2D particle motion for a fully developed velocity flow and particle momentum and sedimentation

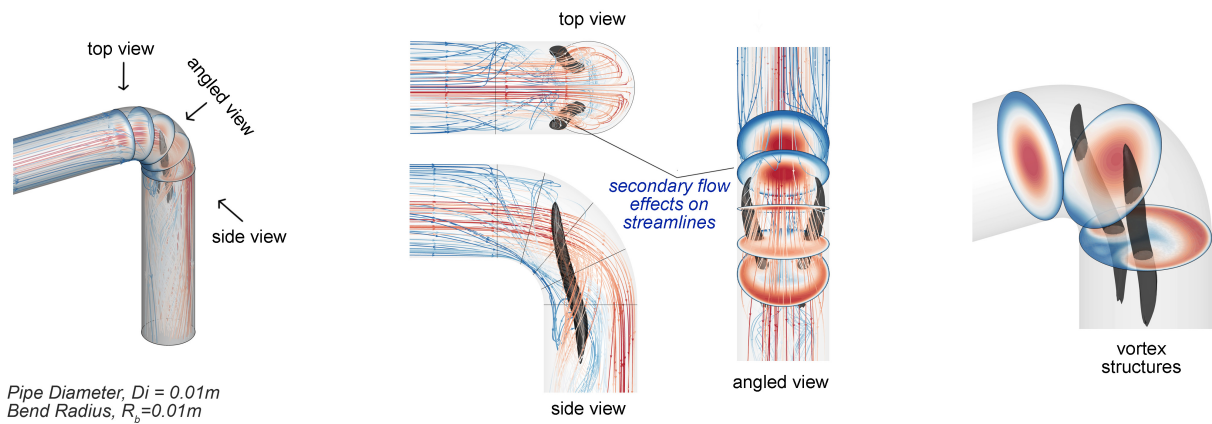


(a) Line A-A' velocity profile

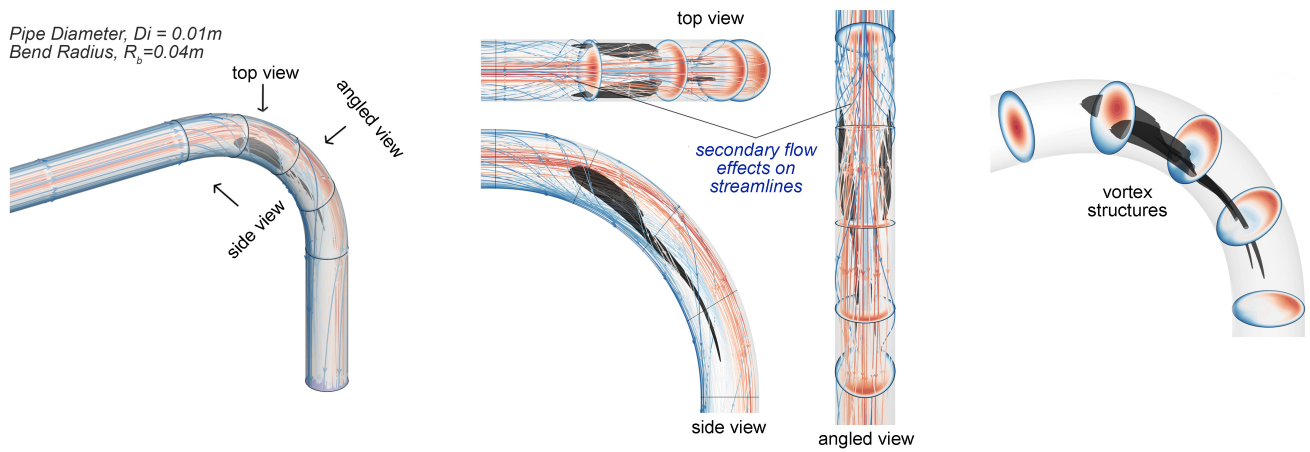


(b) Line B-B' velocity profile

Figure 3: Radial velocity magnitude line profiles taken at $\theta = 45^\circ$ and $\theta = 90^\circ$ in the (a) x-coordinate (Line A-A'), and (b) y-coordinate (Line B-B')



(a) Pipe Diameter, $D_i = 0.01\text{m}$; Bend Radius, $R_b = 0.01\text{m}$, $De = 707$



(b) Pipe Diameter, $D_i = 0.01\text{m}$; Bend Radius, $R_b = 0.04\text{m}$, $De = 354$

Figure 4: Flow streamlines, contours, and vortex cores affected by radius of curvature for pipe diameter = 0.01 m, and $Re=1000$, for $R_o = 2.0$ (sharp bend) and $R_o = 8.0$ (longer bend)

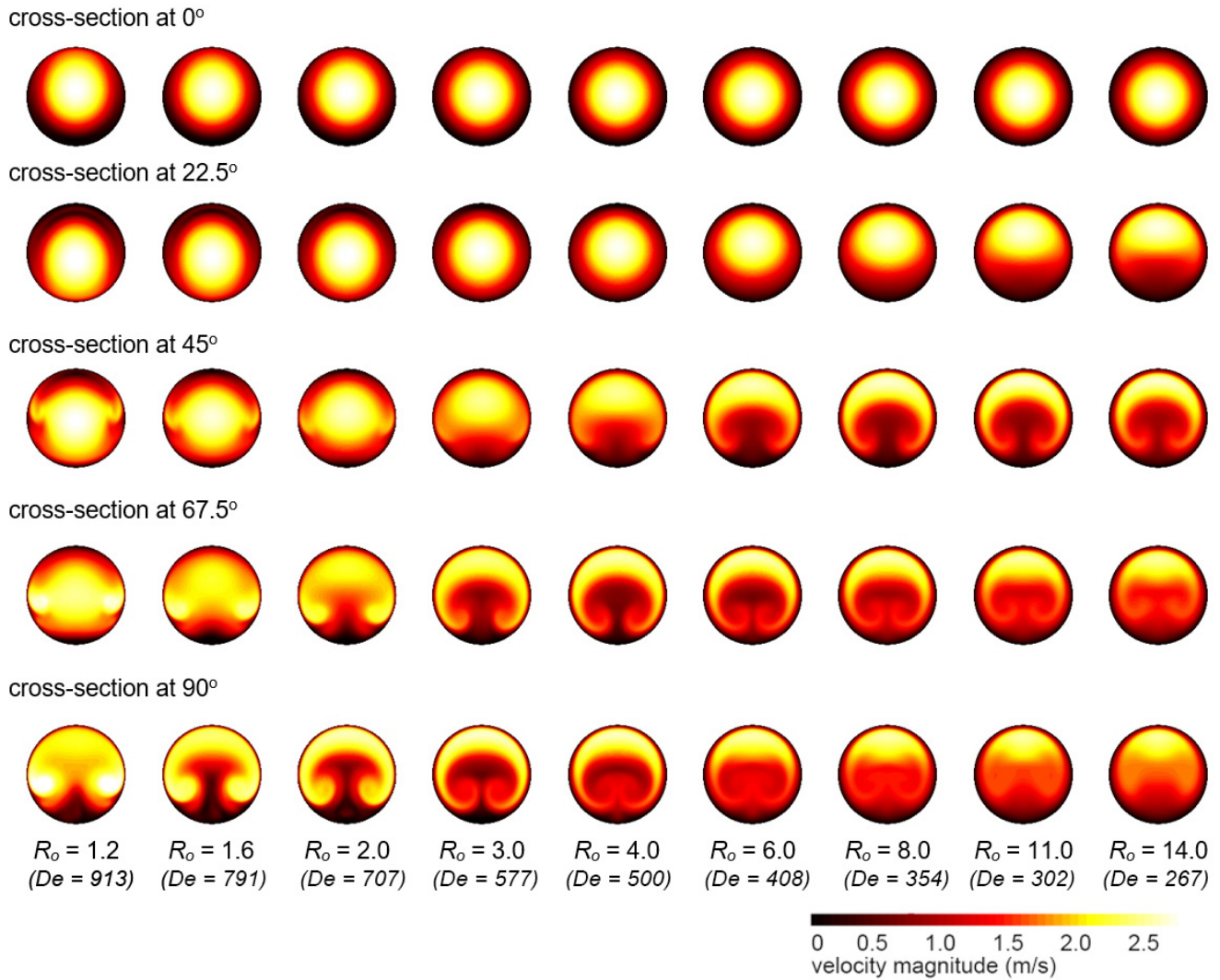
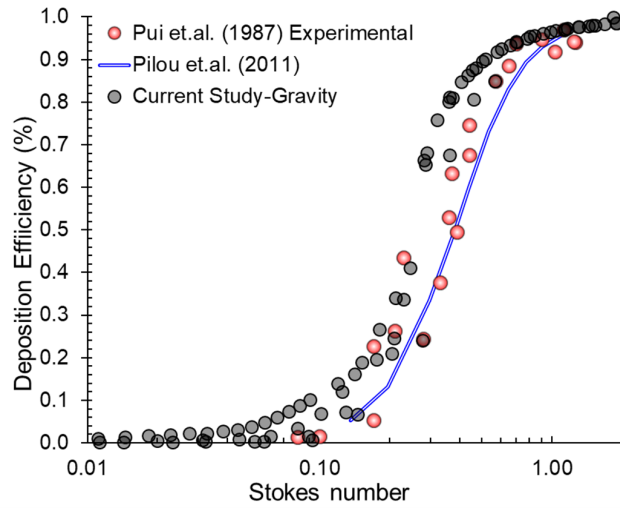
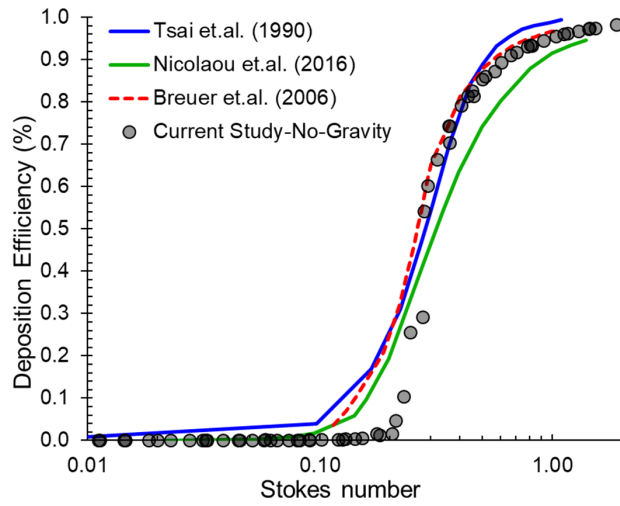


Figure 5: Schematic of the circular pipe bend geometry for all cases where R_b and the pipe diameter, D varied. (b) Pipe bend geometry comparison for $R_b = 2.8D$, and $1.0D$. (c) Structured mesh on the external wall surface. (d) Internal (cross-section) mesh which used O-grid block meshing, and concentration of cells near the wall.



(a) Deposition Efficiency with Gravity



(b) Deposition Efficiency without Gravity

Figure 6: Deposition efficiency profile for $Re=1000$, and $R_o = 5.6$, compared against studies in literature (a) with gravity, (b) without gravity.

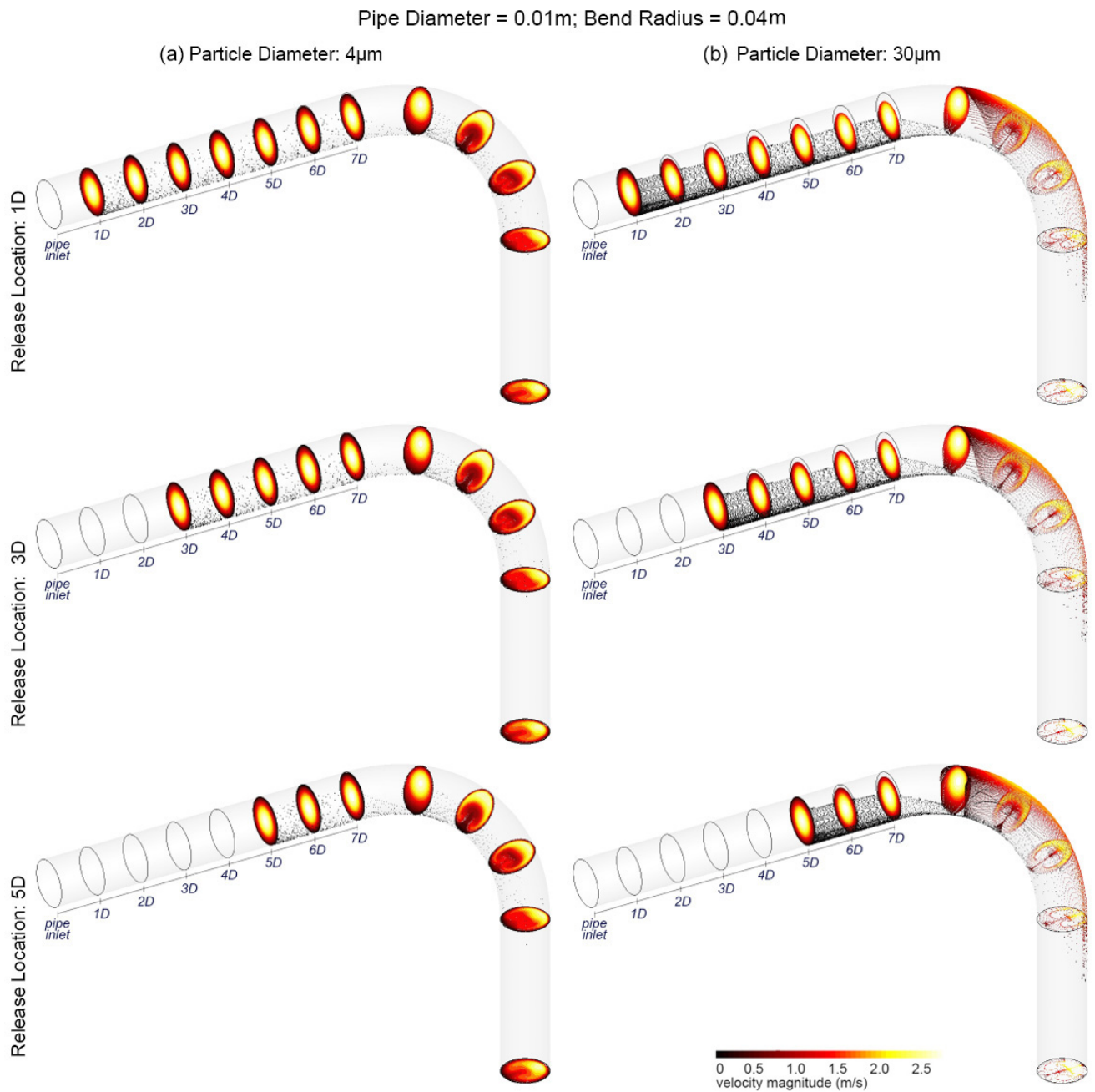


Figure 7: Deposition of 4 μ m and 30 μ m particles in a pipe with pipe diameter $D = 0.01$ m, bend radius $R_b = 0.04$ m, and $Re = 1000$.

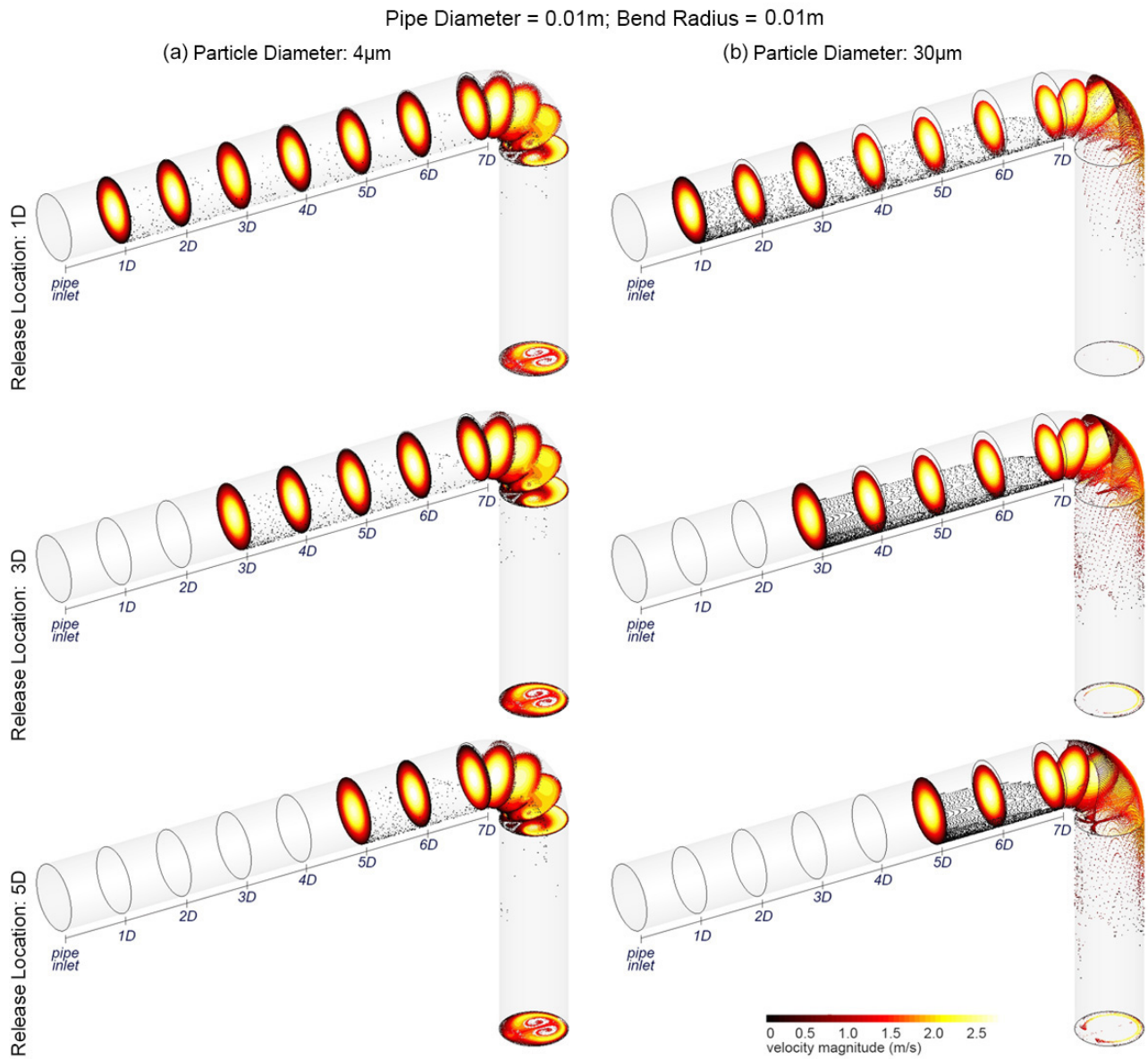
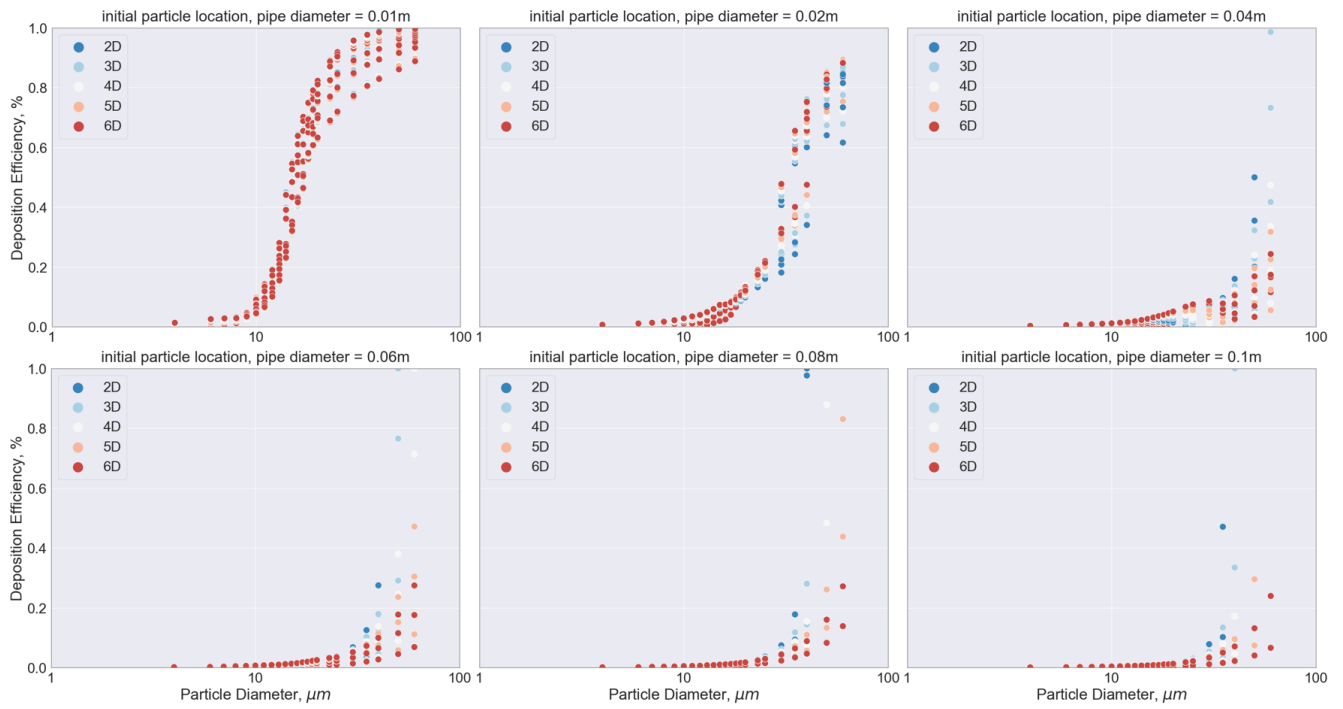
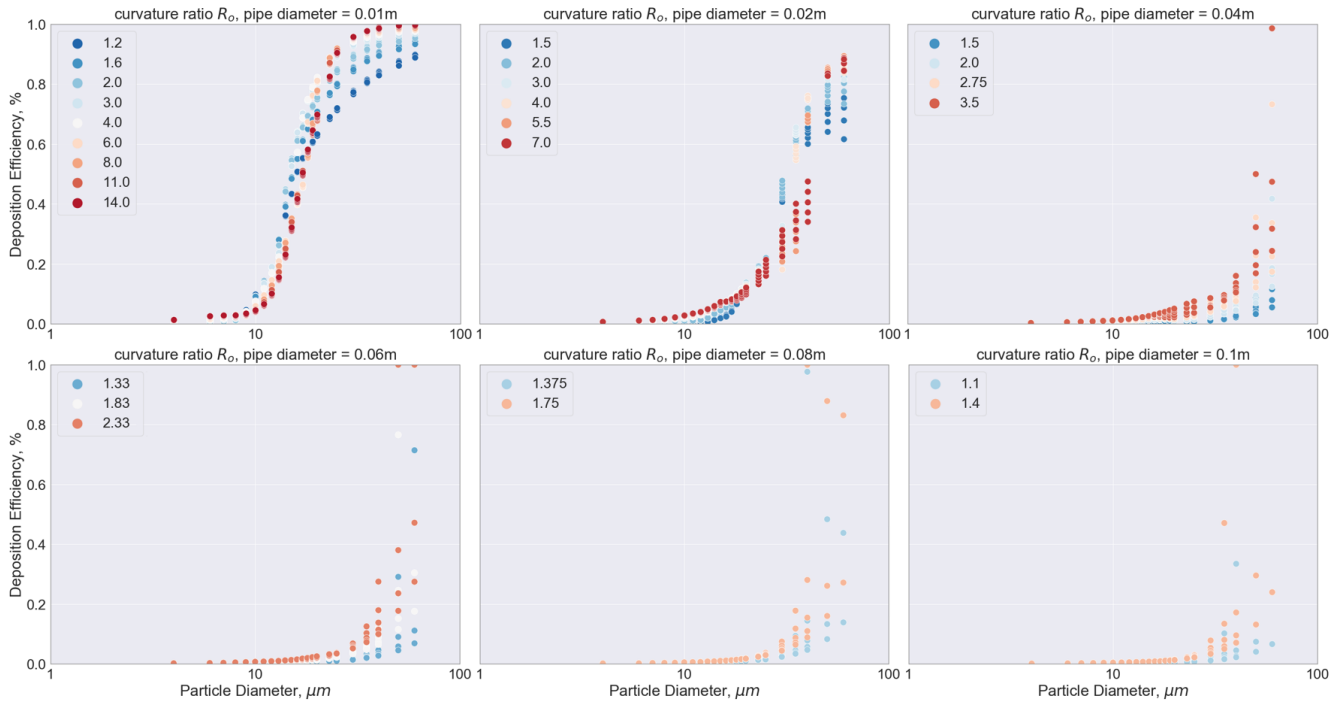


Figure 8: Deposition of 4 μ m and 30 μ m particles in a pipe with pipe diameter $D = 0.01$ m, bend radius $R_b = 0.01$ m, and $Re = 1000$.



(a) Deposition efficiency coloured by initial particle release location



(b) Deposition efficiency coloured by curvature ratio

Figure 9: Deposition efficiency on the pipe bend wall, due to (a) particle release location; and (b) bend curvature ratio

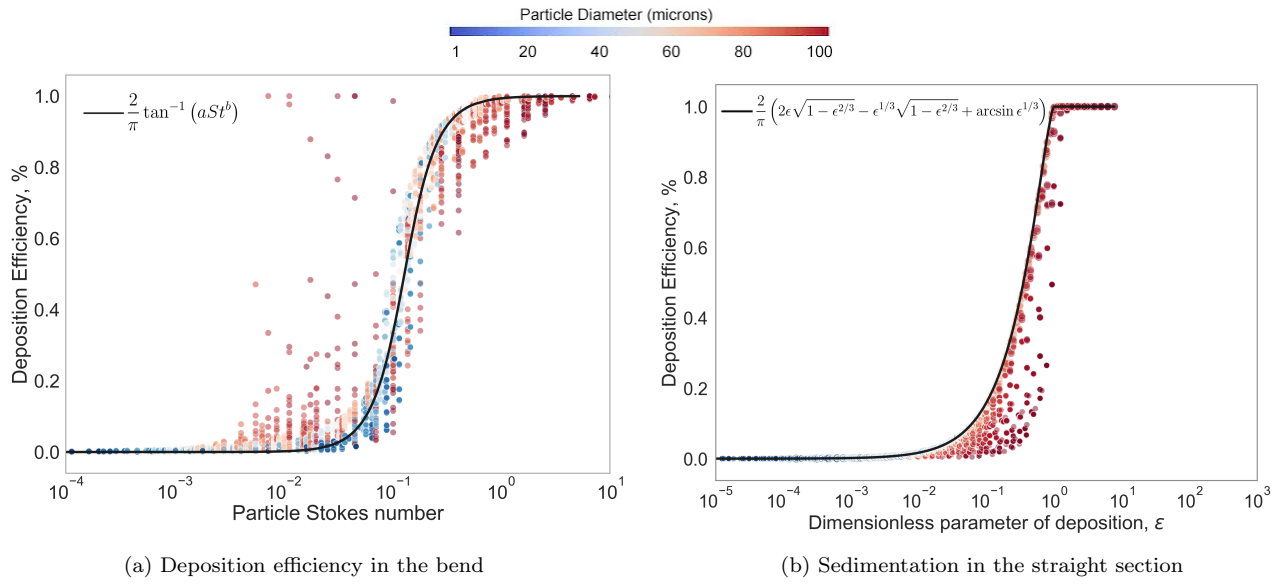


Figure 10: Deposition efficiency for all Dean numbers for (a) bend where $St = \tau U_0 / r$ (Inthavong (2019)); and (b) sedimentation in the straight section where $\epsilon = \frac{3}{4} \frac{V_s}{D} \frac{L}{U}$. In both plots, the data points are semi-transparent and coloured by particle diameter, and therefore multiple data points that overlay on each other create a darker shade, while data points that are outliers are a lighter shade.

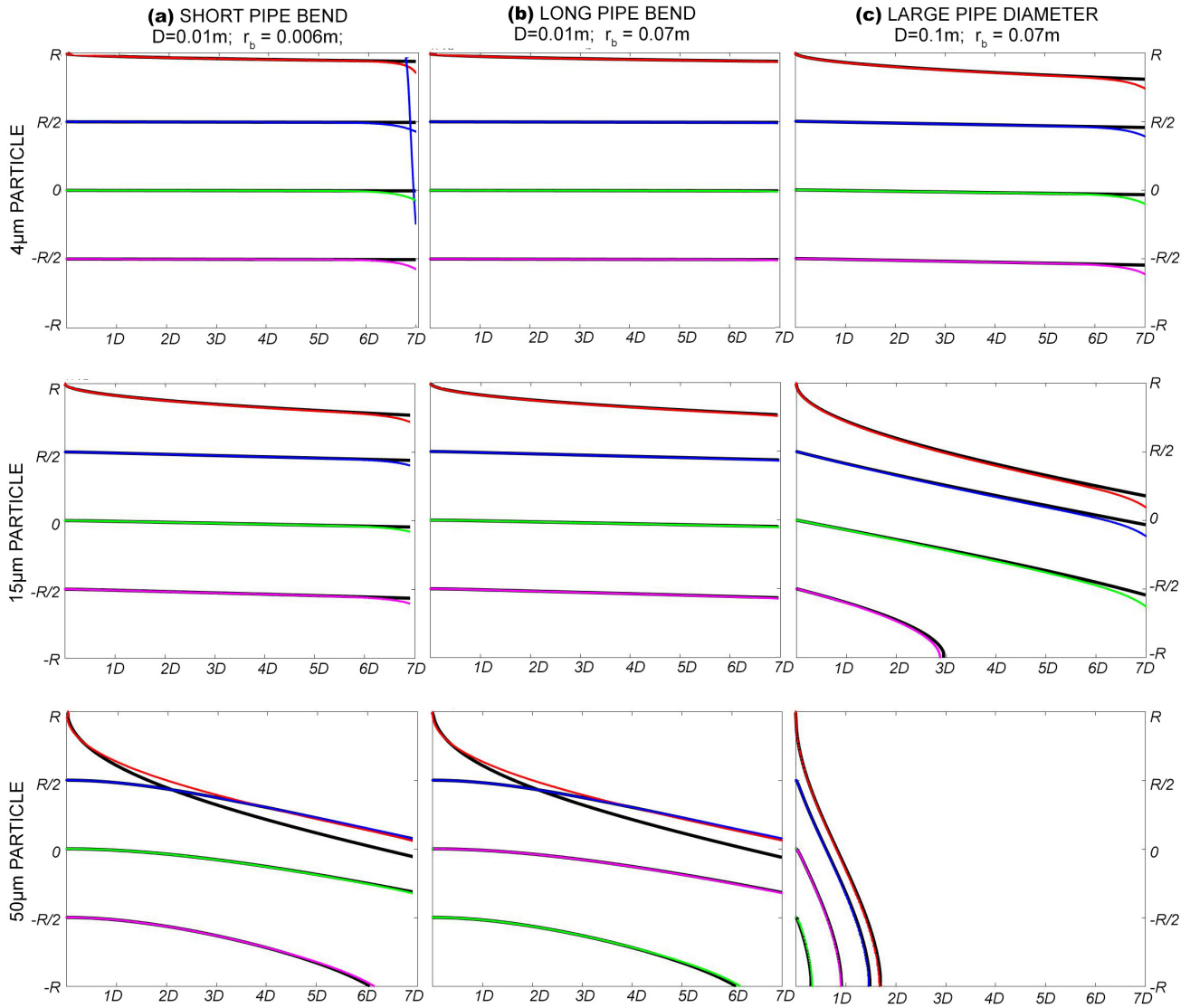


Figure 11: Comparison between analytical solution and simulation results (black lines) for particle trajectories in the straight pipe inlet section released from the inlet for (a) a short pipe bend with pipe diameter = 0.01m, and bend radius = 0.006m; (b) a long pipe bend with pipe diameter = 0.01m, and bend radius = 0.07m; and (c) a large pipe diameter with pipe diameter = 0.1m, and bend radius = 0.07m.